Post doped nitrogen-decorated hollow carbon spheres as a support for Co Fischer-Tropsch catalysts

Mbongiseni W. Dlamini[a,b], Tumelo N. Phaahlamohlaka[a,b], David O. Kumi[a], Roy Forbes[a,b], Linda L. Jewell[b,c], Neil J. Coville[a,b,]

[a] Molecular Sciences Institute, School of Chemistry, University of the Witwatersrand, Johannesburg 2050, South Africa
[b] DST-NRF Centre of Excellence in Catalysis (c*change), University of the Witwatersrand, Johannesburg 2050, South Africa
[c] Department of Chemical Engineering, University of South Africa, Florida Campus, Johannesburg 1710, South Africa

ARTICLE INFO

Keywords:
Nitrogen doping
Fischer-tropsch synthesis
Hollow carbon spheres
Co catalyst
Post doping

ABSTRACT

In this study the outer surface of porous hollow carbon spheres (HCSs) materials were functionalized by N-doping using a post-synthesis method and they were used as a Fischer-Tropsch catalyst support. Melamine was used as the nitrogen source, and carbonization was performed at different temperatures (600 and 900 °C) to introduce variable levels of N into the HCSs, with different bonding configurations. This procedure allowed for the incorporation of up to 13% N. Our results show that post-synthesis N-doping introduced marginal defects into the carbon framework and this did not affect the thermal stability of the materials. XPS studies revealed that the surface content on these materials varied and provided evidence for temperature-tunable bonding config-urations. Effects associated with post-synthesis N-doping were apparent on the Co catalyst (~10 wt.%) properties such as the inhibited reduction caused by a metal-support interaction observed by the H_2-TPR and in situ PXRD techniques. As a consequence the Fischer-Tropsch performance was influenced as both the activity and stability were improved on the catalysts supported on the N-doped materials. TEM analysis of the spent catalysts de-monstrated the influence of N-doping on the sintering characteristics of Co, with particles > 30 nm measured on the N-free catalyst while N-doped samples had sizes < 15 nm.

1. Introduction

Global energy demands have been increasing steadily, with even faster rises seen in emerging economies such as South Africa, India, China and Brazil. Crude oil-derived liquid fuels are the overwhelming source of energy in the world's current transportation structure but the price of crude-oil is unstable as it is also influenced by economic and political factors. [1] As an alternative, the Fischer-Tropsch (FT) synthesis is at the heart of a feasible gas-to-liquids technology aimed at producing clean transportation fuels and building-block chemicals from non-petroleum carbon resources such as coal, natural gas or biomass. [2,3] FT catalysts typically consist of Fe or Co particles dispersed on metal oxides like TiO_2, Al_2O_3, ZrO_2 or SiO_2 which provide excellent thermal stability and mechanical integrity [4]. Despite its higher cost, supported cobalt is preferred over iron catalysts for the FT reaction when the emphasis is on making fuels, due to its high per pass activity, high C_{5+} selectivity, longer catalyst lifetime, low oxygenate and CO_2 selectivity and at present it accounts for a combined estimated world production capacity of 250 000 barrels per day. [5–9] Supporting cobalt on metal oxides usually achieves high dispersions, but the for-mation of hard-to-reduce small Co nanoparticles and mixed compounds (such as Co_2AlO_4, $CoTiO_4$ or Co_2SiO_4) can result in under utilization of Co because of the strong metal-support interactions associated with these materials.

Recently, carbon-based materials have been successfully employed as model support materials for cobalt FT catalysts due to their unique properties, such as a tunable surface area, high thermal stability and tailorable surface chemistry. [10] The properties of carbon materials are strongly influenced by their morphology. [11] Carbon morphologies extensively investigated as catalyst supports include materials such as carbon spheres, carbon nanotubes, carbon nanofibers, carbon nano-coils, carbon nanowires, graphene, bamboo-like carbon and diamond-like carbon. [12–14] Hollow carbon spheres (HCSs) are particularly interesting because of their porous structure, high surface area and low densities. [15,16] The low densities of HCSs coupled with their high surface to volume ratios make them ideal support materials for the synthesis of highly dispersed catalysts. Additionally, the relatively inert carbon framework provides an ideal platform for studies on metal-

Corresponding author at: Molecular Sciences Institute, School of Chemistry, University of the Witwatersrand, Johannesburg 2050, South Africa. E-mail address: neil.coville@wits.ac.za (N.J. Coville).

support interactions, catalyst size effects and the influence of surface functionalization. [17]

The surface chemistry of carbon materials can be tailored by doping them using a heteroatom such as nitrogen, boron or oxygen. Nitrogen doped carbons have displayed superior activity when compared to oxygen-functionalized carbons when used as supports for Fischer-Tropsch catalysts. It has been reported that nitrogen-doped carbons generate a favourable metal-support interaction, resulting in improved catalyst performance. [18,19] Three effects are believed to result in the improved performance of N-doped catalyst supports: (1) modified nu-cleation and growth kinetics during catalyst nanoparticle deposition, which favours the formation of smaller catalyst particle sizes and therefore gives increased dispersion, (2) an increased metal-support interaction which can lead to improved catalyst stability during the reaction, and (3) modification of the electronic structure of the catalyst nanoparticles, which might enhance the intrinsic catalytic activity. [20] N-doping has been shown to increase the catalytic performance of FT catalysts supported on CNTs, [21–23] CSs [24] and more recently graphene. [25,26] However, most of these carbons were functionalized via in situ N-doping. Maldonado and Stevenson have demonstrated that in situ N-doping of CNFs can decrease the thermal stability of N-CNFs by ~90 °C relative to the pristine material due to increased disorder of the carbon framework. [27]

Recently, N-doped carbons in which the doping was done by a post-synthesis methodology have been shown to give an excellent support material. This is partly attributed to the better mechanical and thermal stability of the post-doped carbons. In a typical post-doping procedure, carbon materials are treated with a nitrogen-containing precursor, such as ammonia, acetonitrile or melamine at high temperatures, which decomposes the precursor to give free radicals like NH_2, NH, atomic nitrogen and hydrogen. The free radicals then attack the carbon matrix to form nitrogen-containing functional groups such as –CN, -NH_2, pyrrolic and quaternary nitrogen. [28] For example, Xiong et al. passed acetonitrile over pre-synthesized CNTs at different temperatures (700–900 °C) to prepare a post-doped N-CNT support material, later used to prepare a highly active Fe/N-CNTs Fischer-Tropsch catalyst. [29] In this study we wished to explore the effect of post-synthesis N-doping of HCSs. Here the effect of post doping on the porosity as well as the strength/stability of the HCSs was studied. The N doped HCSs were also used as a support material for Co FT catalysis after the catalysts were prepared under the reaction conditions (high temperature, pres-sure).

2. Experimental methods

2.1. Chemicals

Tetraethyl orthosilicate (TEOS, Sigma-Aldrich), ammonia solution (25%), absolute ethanol (99.6%), resorcinol (Merck), formaldehyde, hydrofluoric acid (HF, 10%), melamine, methanol, cobalt nitrate (Sigma-Aldrich), urea (Promark Chemicals) were obtained from the sources listed and used as received.

2.2. Synthesis of hollow carbon spheres (HCSs)

HCSs were synthesized with a thin shell by the hydrothermal method, utilizing silica as the template. The solid template was made using a modified Stöber method. [30,31] HCS synthesis started with the fabrication of core-shell SiO_2@RF composites. In a typical synthesis, 2.13 mL TEOS was mixed with 37.5 mL of absolute ethanol. This solu-tion was then added to a mixture containing ethanol (25 mL), deionized water (7.5 mL) and ammonia (5 mL). The contents were stirred for 1 h to allow for the formation of colloidal silica spheres (d: 320 nm) which were used as a template. Subsequently, resorcinol (0.5 g) and for-maldehyde (0.7 mL) were added to make the core-shell structures. The solution was stirred for 24 h at room temperature, and then transferred into a Teflon-lined stainless steel autoclave, hydrothermally treated at 100 °C for 24 h. The product was washed/centrifuged successively with water and ethanol, followed by drying at 70 °C for 12 h. Carbonization of the composites was done at 900 °C for 1 h under N_2 (20 mL/min), followed by etching of the silica core using a 10% HF solution to give pristine HCSs (shell: 30 nm).

2.3. Synthesis of nitrogen-doped hollow carbon spheres (N−HCSs)

N−HCSs were prepared following a post synthesis procedure. The core-shell SiO_2@RF composites were fabricated as described above and were then mixed with melamine which was used as the nitrogen pre-cursor. In particular, 2.82 g of melamine was allowed to dissolve in methanol (200 mL) and then 4.7 g of the SiO_2@RF composite was added to the solution under stirring. The mixture was stirred at room temperature and the methanol was then allowed to evaporate. Subsequently, the SiO_2@RF-melamine composites were carbonized under N_2 (20 mL/min) for 1 h. Carbonization was done at two tem-peratures; 600 and 900 °C. The samples were then etched using a 10% HF solution to give N-doped HCSs which are labelled as N−$HCSs_{600}$ and N−$HCSs_{900}$ in accordance with the 600 and 900 °C carbonization temperatures used.

2.4. Catalyst preparation

The Co/C catalysts were prepared with a 10 wt.% loading of the active phase by utilizing the homogeneous deposition precipitation procedure. Three different carbon supports were used; pristine hollow carbon spheres (HCSs), N-doped hollow carbon spheres carbonized at 600 °C (N−$HCSs_{600}$) and N-doped hollow carbon spheres carbonized at 900 °C (N−$HCSs_{900}$). The corresponding Co catalysts prepared from these supports are labelled as 10Co/HCSs, 10Co/N−$HCSs_{600}$ and 10Co/N−$HCSs_{900}$, respectively. All the preparations involved the use of urea as the precipitating agent and cobalt nitrate [$Co(NO_3)_2.6H_2O$] as the metal precursor. In a typical synthesis, the prepared carbon support was dispersed in 200 mL deionized water in a round-bottom flask and the temperature was raised to 90 °C. A solution composed of calculated amounts of the cobalt precursor and urea (1.5 mol urea per mole of metal) dissolved in deionized water (20 mL) was then added drop-wise under continuous stirring. The hydrolysis of urea was al-lowed to proceed under these conditions for 12 h, after which the sol-vent was removed under vacuum in a rotary evaporator at 70 °C. Subsequently the catalyst was calcined at 300 °C for 4 h under a flow of N_2.

2.5. Catalyst characterization

Ex situ powder X-ray diffraction (PXRD) measurements were per-formed on a Bruker D2 phaser with Co Kα radiation (λ = 0.178897 nm), scan range 10-90° (2θ) with 0.026° steps. The in-strument was operated at 30 kV and 10 mA. Indexing the compounds detected by the PXRD technique was achieved using the EVA program. Scanning electron microscopy (SEM) and energy dispersive X-ray spectroscopy (EDX) analysis was done on an FEI Nova Nanolab 600 instrument. TEM analysis was performed on a FEI Tecnai T12 Spirit electron microscope operating at an accelerating voltage of 120 kV. Sample preparation for TEM measurement was achieved by dispersing the powdered samples in ethanol followed by ultrasonication for 3–5 minutes. The suspension was then added drop-wise to carbon-coated Cu grids prior to measurement. Bright-field TEM images were recorded with a CCD detector.

Nitrogen adsorption measurements were carried out on a Micromeritics Tristar 3000 analyser operated at −196 °C. Prior to analysis, accurately weighed samples (200–250 mg) were degassed at 150 °C under N_2 flow for 12 h. Pore size distributions were determined by the BJH (Barrett-Joyner-Halenda) method while pore volumes were

calculated at a relative pressure of 0.995 (P/P_o) by assuming that the pores were filled with the condensate in the liquid state. Raman spec-troscopy analysis was carried out on an InVia Raman spectrometer fitted with a DuoScan attachment. The spectra were recorded at a laser wavelength of 514.5 nm and the power at the sample was 0.2 mW. X-ray photoelectron spectroscopy (XPS) measurements were done on a SHIMADZU KRATOS analytical AXIS SUPRA™ XPS system with mono-chromatic Al K_α radiation (1486.6 eV). The working pressure in the measurement chamber was kept at 1.8×10^{-8} torr.

H_2-temperature programmed reduction (TPR) experiments were done on a Micromeritics Autochem II instrument fitted with a thermal conductivity detector (TCD). Samples were outgassed in Ar at 150 °C for 30 min prior to the analysis with 5% H_2 balance Ar in the temperature range 50–900 °C. Brooks mass flow controllers were used to maintain the flow rate at 45 mL/min during the analysis. The reducibility of the catalyst was also monitored by the in situ PXRD technique. A Bruker D8 Advance AXS diffractometer fitted with an Anton Paar XRK 900 reac-tion chamber was used for data collection. The diffractometer was operated at 40 kV, 40 mA and used a Cu radiation source ($\lambda_{K\alpha}$ = 0.154084 nm). Variable temperature measurements were done in the range 150–550 °C using 50 °C step-wise increments; subsequently the temperature was maintained at 550 °C for 2 h. Phase information was recorded on a VÅntec position sensitive detector in the 2 theta range 15-80°. The Rietveld refinement method incorporated in the TOPAS 4.2 (Bruker AXS) software package was used to analyse the in situ PXRD data.

2.6. Catalytic evaluations

Synthesis gas conversion was performed in a fixed-bed stainless steel reactor (i.d. = 16 mm) that was heated using a tube furnace and a thermocouple which was inserted into the accurately weighed catalyst bed (0.5 g, 90–150 μm). Prior to FT synthesis, the catalyst was reduced in situ in pure hydrogen at 2 bar, with a gas flow rate of 45 mL/min, at 350 °C for 18 h; the heating rate was 1 °C/min. The reactor temperature was then dropped to 220 °C before introducing syngas. The following conditions were employed for FT catalytic evaluations, i.e., 220/250 °C, 10 bar, synthesis gas composition: 60 vol% H_2, 30 vol% CO and 10 vol% N_2 (internal standard). The composition of the gaseous reactor effluent was analysed on two online gas chromatographs fitted with TCD and FID detectors. The gas lines between the reactor and the GCs were kept at 150 °C to prevent the condensation of water and long-chain hydro-carbons. Liquid products were collected in separate hot and cold traps, installed below the reactor, and maintained at 150 and 20 °C, respec-tively.

3. Results and discussion

3.1. Synthesis and doping of hollow carbon spheres (HCSs)

A three-step approach was utilized in the synthesis of the porous catalyst carrier. First, pre-fabricated Stöber silica spheres were coated with a thin layer of a resorcinol-formaldehyde resin to yield SiO_2@RF composites. Second, the polymeric resin was converted to a layer of carbon via a carbonization procedure performed at 900 °C under inert conditions. This step led to the conversion of the brownish composite to a black powder represented as SiO_2@C. In the final step, the silica core was etched out using HF to yield the HCSs.

Shown in Fig. 1 are TEM and SEM images of the SiO_2 spheres, SiO_2@RF composites and HCSs made in the study. The synthesized Stöber spheres (diameter: 320 ± 20 nm) were highly uniform and monodisperse, possessing an outer surface that is smooth and well de-fined. Electron microscopy images (Fig. 1c–d) show that the SiO_2@RF composite consists of a silica core that is encapsulated by a uniform carbon shell (thickness: 30 ± 5 nm). The HF etching of the silica template yielded monodispersed pristine HCSs (Fig. 1e–f). This etching

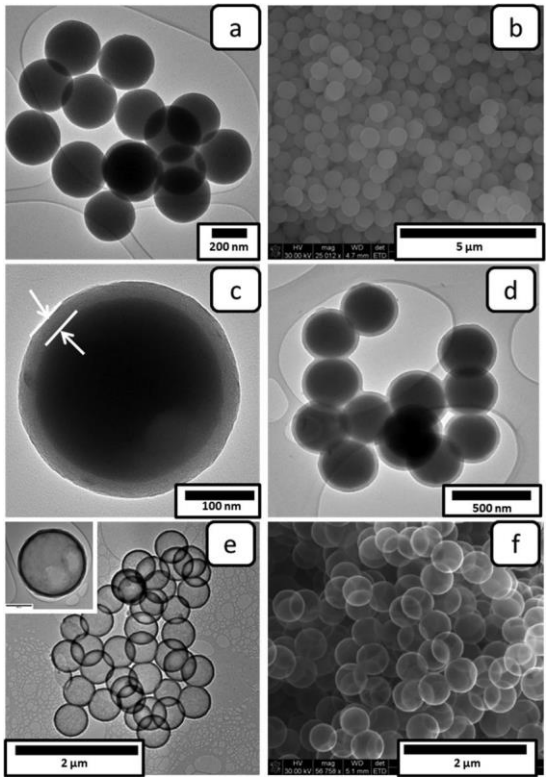

Fig. 1. TEM and SEM images of (a,b) Stöber silica spheres, (c,d) egg-yolk SiO_2@ RF composites and, (e,f) hollow carbon spheres. The insert in Fig. 1e shows a single hollow carbon sphere (HCS).

process did not affect the carbon shell thickness, as expected. Synthesis of N-doped HCSs was achieved through a similar protocol as that used to make the pristine HCSs but with slight variations. After the synthesis of the SiO_2@RF composite, melamine (dissolved in me-thanol) was added to functionalize the outer surface on the carbons with nitrogen. The materials were then carbonized in N_2 at either 600 or 900 °C to yield N−$HCSs_{600}$ and N−$HCSs_{900}$, respectively. CHNS elemental analysis was used to quantify the total nitrogen content on the materials after the carbonization steps and the results are presented in Table 1. The samples that were carbonized at 600 °C had a nitrogen content of 13.1% while a lower N content of 5.4% was recorded after the 900 °C heat treatment procedure. The reduced nitrogen content at higher temperatures is attributed to the cleavage of CeN bonds at the higher temperature. [32,33]

Raman spectroscopy is a useful and non-destructive technique for studying the structure and quality of carbonaceous nanomaterials. Analysis of the ratio of D band to G band intensities (I_D/I_G) from the Raman spectra of HCS, N−$HCSs_{600}$ and N−$HCSs_{900}$ (Fig. S1) allowed an investigation of bonding features of the carbon spheres. It can be seen from the spectra that the I_D/I_G ratio marginally increased on the N-doped samples (Table 1, Fig. S1), suggesting that the intercalation of N atoms into the carbon framework increased structural defects in the material. [34] Correspondingly, the D-band position is blue shifted in

Table 1
Elemental nitrogen content and Raman spectroscopy data of the pristine hollow carbon spheres (HCSs) and the N-doped materials carbonized at 600 and 900 °C.

Sample	% N content (CHNS)	I_D/I_G	D band position (cm^{-1})	G band position (cm^{-1})
HCSs	Not detected	0.98	1345	1593
N-$HCSs_{600}$	13.1	1.01	1369	1593
N-$HCSs_{900}$	5.4	1.00	1356	1593

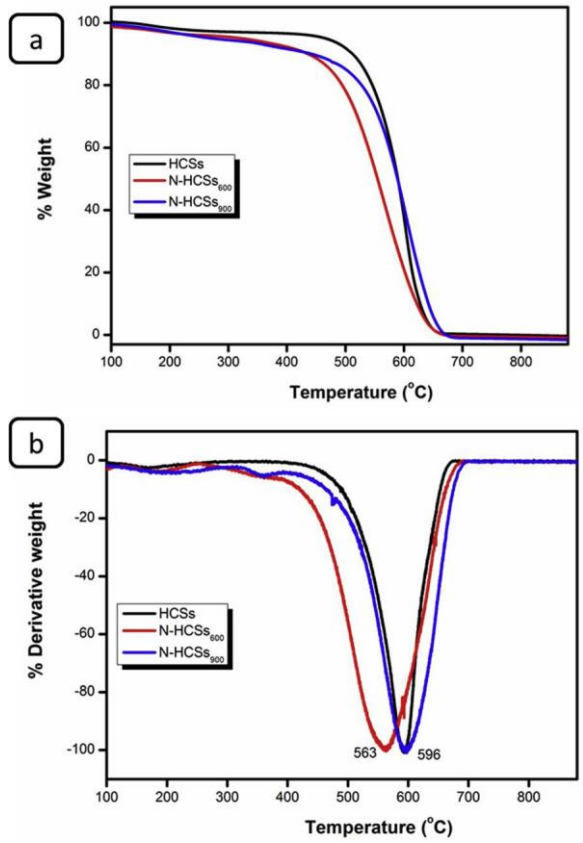

Fig. 2. (a) TGA and (b) DTA profiles of the pristine HCSs, N−HCSs$_{600}$ and N−HCSs$_{900}$.

the N-doped samples relative to the N-free HCSs. The magnitude of the blue shift is related to the surface nitrogen concentration. This shift confirmed the incorporation of N atoms into the carbon framework, and is analogous to hole doping that was noted to lead to an increase of the D-band frequency of graphene, quantum dots and carbon nanotubes. [35–37] The G-band peak positions remained relatively unchanged even after N-doping.

Effects associated with post-synthesis N-doping on the thermal sta-bility of the carbon supports were studied using thermogravimetric analysis (TGA). The synthesized pristine HCSs were seen to be highly stable in an oxidizing environment with a single decomposition peak at 596 °C (Fig. 2). This peak is attributed to the oxidation of carbon to carbon dioxide. The N-doped carbon materials also displayed good thermal stabilities with major decomposition peaks at 596 and 563 °C for the samples with 5.4 and 13.1% nitrogen contents, respectively. It is to be noted that the major decomposition peak on the N-doped samples demonstrates the absence of residual melamine in the materials. The TGA/DTA profile of melamine is provided in the supporting informa-tion (Fig. S2). The lower thermal stability of the N−HCSs$_{600}$ sample can be associated with two effects; (i) increased defects in the carbon fra-mework due to nitrogen incorporation as also determined from Raman spectroscopy studies, and (ii) the relatively lower carbonization tem-perature (600 °C) used for the preparation of this material. The HCS and N−HCS$_{900}$ materials were carbonized at 900 °C. It was interesting to note that the N−HCSs$_{900}$ had a similar decomposition temperature as found for the pristine HCSs. It was noted that all three samples had no residue after the TGA experiments, and this confirmed that the silica template was completely etched out using the HF acid treatment giving carbons with high purity. In summary, TGA experiments confirmed that these N-doped and N-free HCS materials would be stable at Fischer-Tropsch synthesis reaction temperatures (T < 250 °C).

The doping of carbon materials has been shown to improve the performances of supported catalysts. The common structural compro-mise for materials doped in situ with N is reduced thermal and me-chanical stability. The thermal stability of N-CNTs, N-CNFs and N-CSs doped during synthesis has been shown to decrease by up to 90 °C re-lative to their pristine counterparts due to increased defects within the carbon framework. [27] In this study we found that because the dopant is only introduced after the carbon spheres are already formed, minimum defects are introduced on the carbon structure. The overall change in the I_D/I_G ratio was found to be 0.03, which is very small for samples containing a 13% difference in the heteroatom content. As a consequence of the minimal defects introduced only a small decrease (33 °C) in thermal stability was observed even though a relatively high N content (13.1%) was incorporated into the surface of the carbon material.

3.2. X-ray photoelectron spectroscopy (XPS) analysis

Data measured from X-ray photoelectron spectroscopy (XPS) ex-periments was used to determine the elemental composition and bonding configurations of nitrogen, carbon and oxygen on the carbon supports. As shown on the wide scans in Fig. 3a, the spectra confirmed the presence of N, C and O on the N-doped samples while N was not detected on the pristine HCSs as can be expected. High resolution N 1 s spectra were recorded to characterize the bonding configurations of the nitrogen atoms, shown in Fig. 3b and c. The N 1 s spectra of the N−HCSs were deconvoluted by fitting four Gaussian peaks at 398.4, 400.9, 401.7 and 403.4 eV. [38–40] These peaks are due to pyridinic nitrogen, pyrrolic nitrogen, graphitic or quaternary nitrogen and oxi-dized nitrogen or pyridine oxide, respectively. It is worth noting that the N atom in pyridinic nitrogen has sp^2 hybridization with two neighbouring C atoms, while the N atom in pyrrolic nitrogen is sub-stituted into a five-membered carbon ring. For the peaks with high binding energies, the N atom in quaternary nitrogen has sp^3 hy-bridization with three C atoms attached to the N because it is in-corporated into a graphene layer, while the N atom in oxidized nitrogen is attached to two C atoms and one O atom.

Table 2 summarises the percentage contributions for the different nitrogen bonding configurations after deconvolution of the N 1 s spectra which are presented in Fig. 4. It was observed that increasing the car-bonization temperature from 600 to 900 °C changed the bonding con-figurations of nitrogen atoms on the surface of the hollow carbon sphere support materials. In particular, the pyridinic nitrogen content de-creased from 35.8 to 27.1% at elevated temperatures. The ratios of pyrrolic, graphitic and oxidized nitrogen increased in the N−HCSs$_{900}$ sample relative to data measured for the N−HCSs$_{600}$ support material but the amounts are less.

XPS spectra were also analysed to investigate the effect of post-synthesis nitrogen doping on the bonding configurations of the surface carbon and oxygen atoms. Fig. 4a, c and e shows C 1s spectra of the different carbon supports. The spectra were deconvoluted into three peaks with maxima at 284.6, 285.3 and 287.0 eV, corresponding to different carbon functional groups (Table S1). [41] The peak at 284.6 eV is attributed to pure graphitic carbon sites (C]C, C⌀C, C–H) abbreviated as Type 1-C, the peak at 285.4 eV is due to carbon atoms with sp^2 hybridization (C–O, C–N) and is labelled as Type 2-C, while the peak with a maximum at 287.1 eV is designated to the O]C⌀O and O]C–N surface functional groups (Type 3-C). As shown in Table S1, the N-doped samples display a significant decrease of pure graphitic carbon sites and an increase in the amount of carbon with sp^2 hy-bridization. The sp^2 hybridized sites contain nitrogen groups and this confirms the incorporation of N into the carbon network. This ob-servation is in agreement with Raman data where a slight increase in the sp^2 content was seen (Table 1, Fig. S1). The higher quantities of Type 2-C and Type 3-C on the N−HCSs$_{600}$ sample relative to the N−HCSs$_{900}$ sample are related to the total N content on these mate-rials.

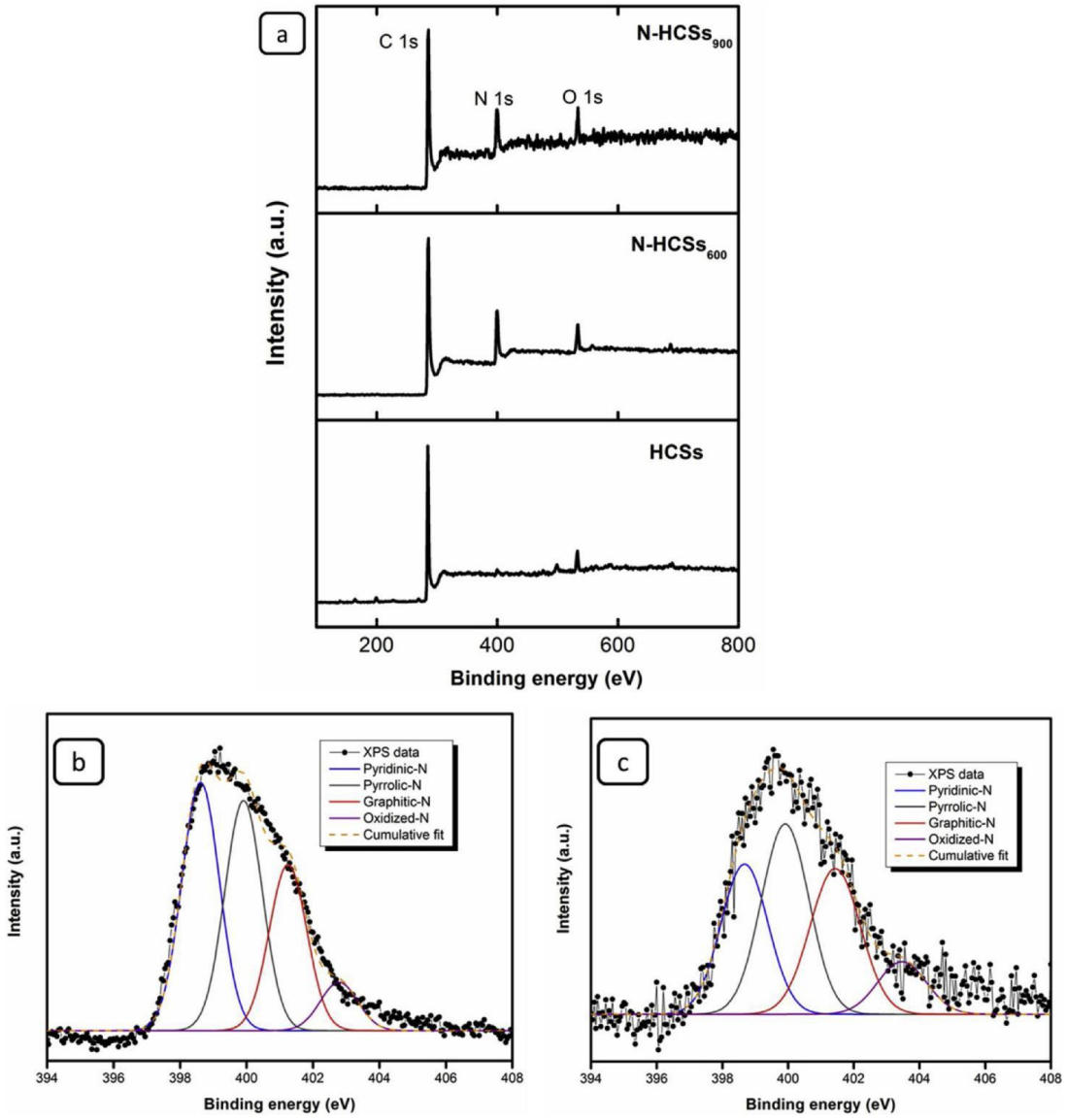

Fig. 3. XPS data measured from the samples, (a) wide scan spectra, and the N 1 s spectra for N-doped hollow carbon spheres, (b) N−HCSs$_{600}$ and (c) N−HCSs$_{900}$.

Table 2
XPS N 1 s spectral parameters from the deconvoluted peaks.

Sample	Nitrogen bonding configurations (%)				R^2 value
	Pyridinic-N	Pyrrolic-N	Graphitic-N	Oxidized-N	
N-HCSs$_{600}$	35.8	33.2	24.0	7.0	0.989
N-HCSs$_{900}$	27.1	34.8	28.2	9.9	0.984

A similar approach was also adopted to deconvolute the XPS spectra of O 1 s, shown in Fig. 4b, d and f into three peaks corresponding to the following functional groups; -C = O (531.0 eV), CeOeC (531.9 eV) and OeC]O (533.0 eV). [42] These three peaks are abbreviated Type 1-O, Type 2-O and Type 3-O, respectively. The contributions of these func-tional groups to the total O content are listed in Table S2. It can be observed from the Table that post-synthesis N-doping favours the CeOeC (Type 2-O) and OeC = O sites, whereas the pristine HCSs display a higher eC]O content (i.e. Type 1-O).

3.3. Textual properties of the support materials

Specific surface areas of the carbon supports were measured by the BET method and the results are tabulated in Table 3. The carbon sup-ports were found to have large surface areas (> 400 m^2/g). In parti-cular, the pristine hollow support had a specific surface area of 507 m^2/ g. Furthermore, incorporation of the nitrogen precursor on the outer surface of the carbons was noted to slightly decrease the surface area, possibly through pore blockage. The low specific surface area measured on the N−HCSs$_{600}$ sample is attributed to the high N content and the low carbonization temperature (600 °C) used. The pore structures of all the materials displayed mesoporous characteristics as their average pore sizes were greater than 2 nm.

3.4. Catalyst characterization

3.4.1. Microscopic analysis

Fig. 5 shows TEM images for the 10Co/HCSs, 10Co/N−HCSs$_{600}$ and 10Co/N−HCSs$_{900}$ catalysts and the corresponding particle size dis-tributions. It can be seen that the cobalt nanoparticles supported on the pristine HCSs had an average particle size of 7.7 nm with particle size distribution shown in Fig. 5b. For the samples supported on the N-

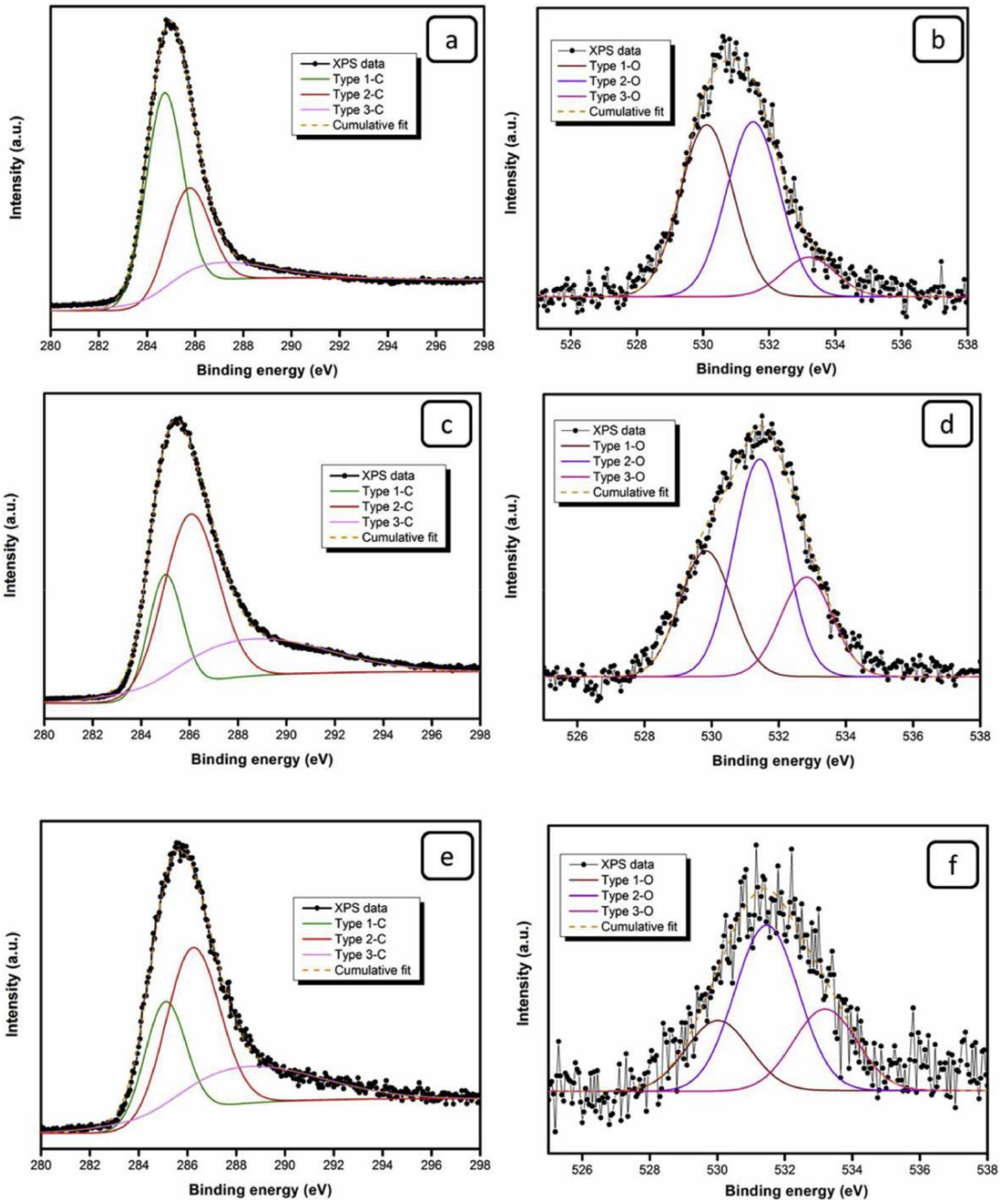

Fig. 4. XPS spectra of C 1 s and O 1 s for the (a–b) HCSs, (c–d) N−HCSs$_{600}$, (e–f) N−HCSs$_{900}$ samples.

Table 3
Summarized textual properties of the carbon supports and the calcined cata-lysts.

Sample name	Textual properties			Co_3O_4 size (nm)[a]
	Surface area (m^2/g)	Pore volume (cm^3/g)	Pore diameter (nm)	
HCSs	507	0.41	3.2	–
N-HCSs$_{600}$	411	0.43	4.6	–
N-HCSs$_{900}$	436	0.36	3.3	–
10Co/HSCs	332	0.35	4.6	8.2
10Co/N-HCSs$_{600}$	266	0.35	4.1	5.0
10Co/N-HCSs$_{900}$	295	0.36	3.6	5.9

[a] Cobalt oxide crystallite sizes were estimated from XRD data using the Scherrer equation.

doped HCSs, it was observed that the average particle sizes were in-versely proportional to the nitrogen content on the support. Hence the 10Co/N−HCSs$_{600}$ sample had the smallest particles (5.6 nm), shown in Fig. 5d, followed by the 10Co/N−HCSs$_{900}$ with an average particle size of 6.4 nm, Fig. 5f. Generally small cobalt oxide particles were seen on all the supports and this is attributed to the low density of the hollow carbon spheres which provides a large surface for the metal precursor deposition. However, the particles appeared to be visually slightly better dispersed on the N-doped supports as determined from the mi-croscopy images (Fig. 5c,e).

3.4.2. Thermal stability of catalysts

Thermogravimetric analysis (TGA) of the catalysts was also carried out to study the influence of cobalt nanoparticles on the thermal sta-bility of the hollow carbon supports. A plot of the TGA derivative curve allowed for the identification of points where maximum weight loss

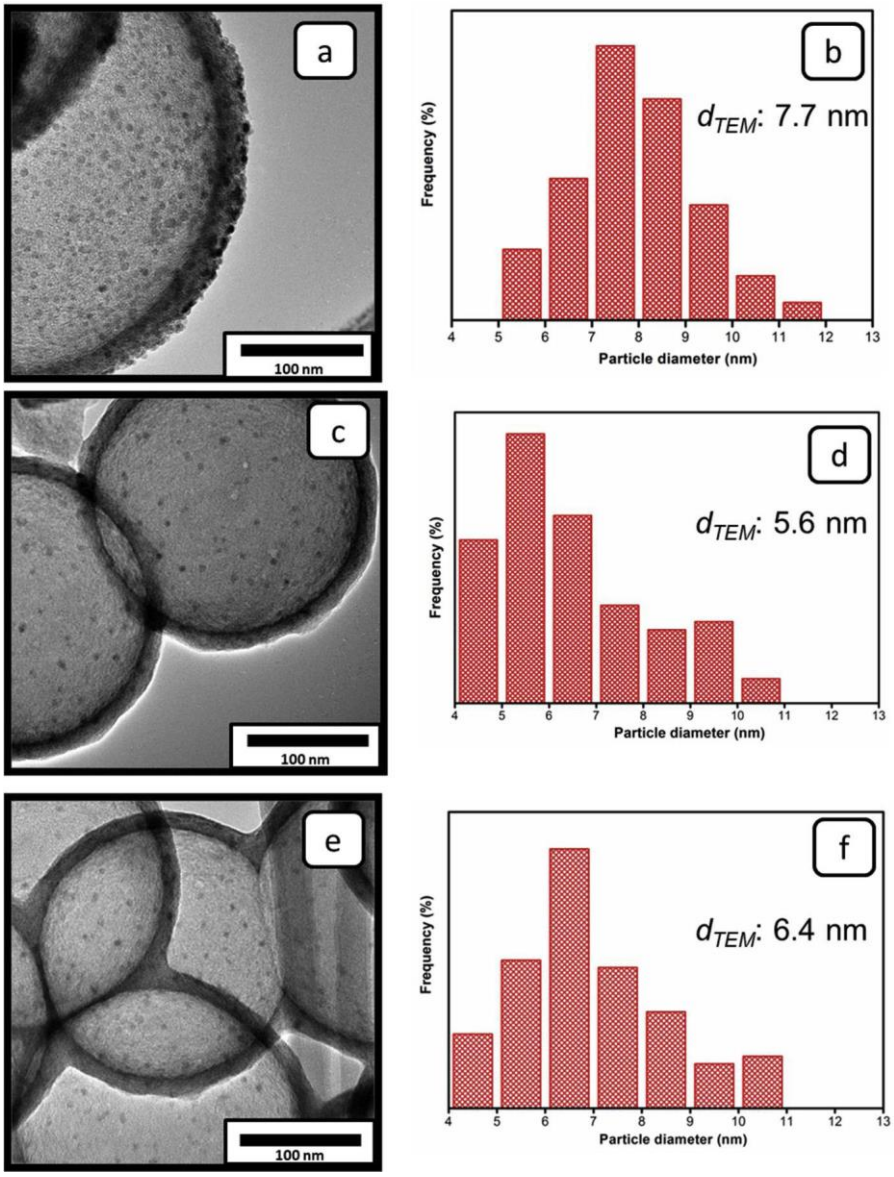

Fig. 5. TEM images and the corresponding Co particle size distributions for (a, b) 10Co/HCSs, (c, d) 10Co/N−$HCSs_{600}$ and (e, f) 10Co/N−$HCSs_{900}$ samples.

occurred during the experiments. Fig. 6 depicts TGA/DTA profiles of the catalysts which were measured in a flow of air using a heating rate of 10 °C/min. As can be seen from the derivative curves in Fig. 6b, the decomposition temperature was less than 480 °C for all the carbon supports after loading cobalt oxide. This is in contrast to oxidation temperatures greater than 560 °C recorded prior to loading the catalyst precursor. The decrease in thermal stability is attributed to cobalt na-noparticles catalysing the oxidation of carbon to carbon dioxide. The decomposition trend of the catalysts was similar to that observed prior to loading the active phase precursor, with the 10Co/N−$HCSs_{600}$ sample having the lowest stability. It should be noted that these cata-lysts (and the supports) are stable within the temperature range at which catalytic FT measurements were performed (220–250 °C). Meanwhile, a residue of about 16% was noted after the TGA experiments and is due to Co_3O_4 which was loaded onto the supports. This percentage residue corresponds to 11.7% Co which was close to the theoretical Co loading of 10 wt.% added onto the hollow carbon spheres.

3.4.3. Powder X-ray diffraction (PXRD)

Ex situ PXRD data of the calcined samples is shown in Fig. 7. The peaks at 2θ positions of 28.2 and 50.6° were present in all the patterns and are attributed to the (002) and (100) diffraction peaks due to graphitic carbon. [43] The 10Co/HCSs, 10Co/N−$HCSs_{600}$ and 10Co/ N−$HCSs_{900}$ samples all displayed peaks at 2θ positions of 21.9, 42.5, 70.0 and 77.2° which are typically indexed as the (111), (311), (511) and (440) diffraction planes of face-centred cubic Co_3O_4 [PDF No. 00-043-1003]. It was therefore concluded that surface nitrogen functio-nalization did not affect the crystallographic phase of the metal pre-cursor as the spinel phase of cobalt oxide was detected in all three samples. Subsequently, the cobalt oxide crystallite sizes were estimated from line broadening analysis using the Scherrer equation and are listed in Table 3. The Co oxide crystallite sizes were seen to vary as a function of the nitrogen content on the carbon support. As can be seen in Table 3, the pristine support had the biggest crystallites with a size of 8.2 nm. The catalyst precursor crystallite sizes decreased with an in-crease in the nitrogen content of the carbon support. For instance, the sizes for the 10Co/N−$HCSs_{600}$ sample were estimated to be 5.0 nm on average. The decrease in Co size with an increase in heteroatom content is consistent with surface nitrogen atoms influencing the nucleation sites for catalyst deposition on the carbon support. It is known that nitrogen-rich carbons provide a range of chemical binding sites for a

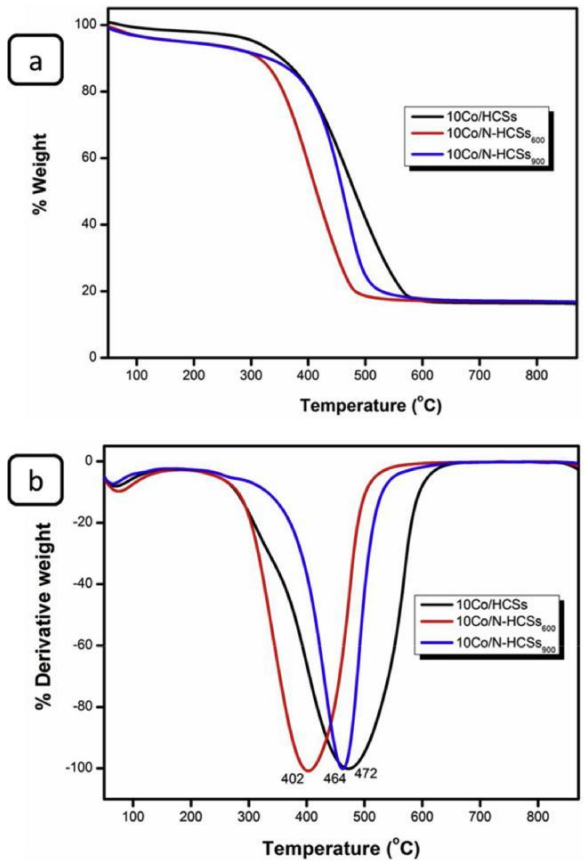

Fig. 6. (a) TGA and (b) DTA profiles for the 10Co/HCSs, 10Co/N−HCSs$_{600}$ and 10Co/N−HCSs$_{900}$ samples.

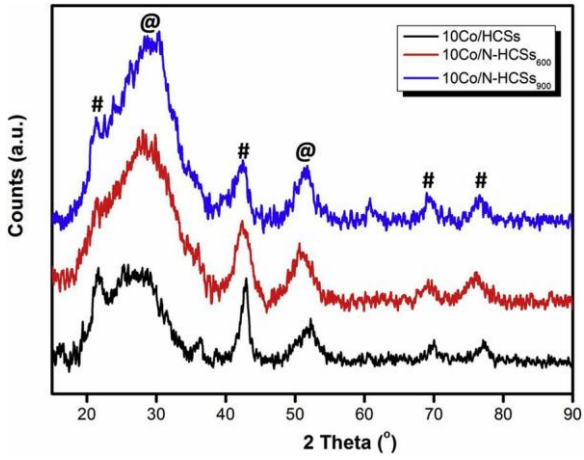

Fig. 7. Ex situ PXRD patterns of the calcined cobalt catalysts supported on pristine and N-doped HCSs. (Carbon: @, Co_3O_4: #).

direct support-metal interaction. Thus, the nanoparticles are anchored to the various binding and nucleation sites, which results in improved dispersion and smaller particles. [19]

3.4.4. BET analysis of the catalysts

Table 3 shows the surface areas, pore volumes and pore sizes of the calcined cobalt on carbon samples as determined by the BET method. It was observed that the specific surface areas decreased upon loading the metal precursors. This trend is to be expected because the metal pre-cursors are loaded on the outer surface of the hollow supports and could thus block some of the mesopores. However, all the measured surface

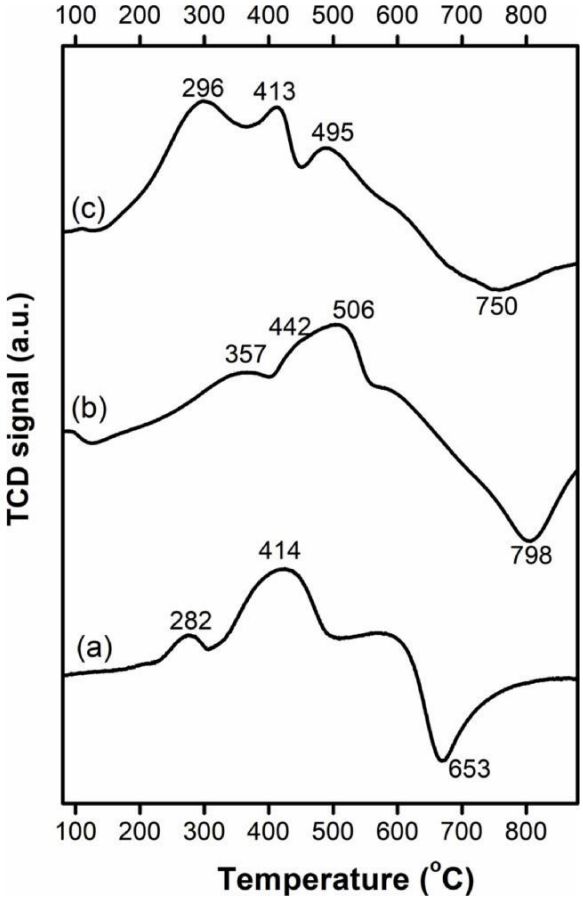

Fig. 8. H_2-TPR profiles for cobalt nanoparticles on various hollow carbon sphere supports, (a) 10Co/HCSs, (b) 10Co/N−HCSs$_{600}$ and (c) 10Co/ N−HCSs$_{900}$.

areas are still relatively high (> 250 m^2/g) and thus ideal for FT cat-alysis. It was interesting to note that the mesoporous nature of the materials was retained on the catalysts as pore sizes greater than 2 nm were again measured on all the samples.

3.4.5. Catalyst reducibility

The effect of N-functionalization on the stepwise reduction of cobalt oxide was monitored by TPR and in situ PXRD techniques. TPR profiles of cobalt nanoparticles on the hollow carbon supports are displayed in Fig. 8 and the observed peak positions are given in Table S3. All sam-ples show the characteristic reduction features of cobalt oxide which are ascribed to the $Co_3O_4 \rightarrow CoO$ and $CoO \rightarrow Co°$ transformations (Eqs. (1) and (2)). [44] The first reduction step ($Co_3O_4 \rightarrow CoO$) occurred at T < 400 °C, with reduction at temperatures around 282, 357 and 296 °C for the 10Co/HCSs, 10Co/N−HCSs$_{600}$ and 10Co/N−HCSs$_{900}$ samples, respectively. This reduction step evidently occurs at higher temperatures for the catalysts dispersed on N-doped hollow spheres which were determined to be smaller in size. A similar behaviour was again displayed during the $CoO \rightarrow Co°$ reduction step with the pristine-supported Co showing a single reduction temperature (414 °C) while Co on the N-doped substrate had the higher reduction temperatures, with reduction at 442/506 and 413/495 °C for the N−HCSs$_{600}$ and N−HCSs$_{900}$ supports. For this reduction step, the peak for the N−HCSs$_{600}$ and the 10Co/N−HCSs$_{900}$ samples was split into two peaks in the 442–506 °C and 413–495 °C regions. The lower temperature signal in the second peak could be due to cobalt nanoparticles which are not in direct contact with N atoms, while the peaks at 495 °C and 506 °C can be assigned to nanoparticles that are in direct contact with N atoms on the support. The differences in cobalt nanoparticle proximity

to N-rich sites are to be expected due to the lower nitrogen content on the N−HCSs$_{900}$ substrate.

$$Co_3O_4 + H_2 \rightarrow 3CoO + H_2O \quad (1)$$

$$CoO + H_2 \rightarrow Co^{\circ} + H_2O \quad (2)$$

It is apparent that N-surface functionalization influenced the re-duction characteristics of supported cobalt oxide nanoparticles, with reduction profiles shifting to higher temperatures with an increase in the nitrogen content. This is attributed to the strong interfacial elec-tronic interaction between cobalt oxide nanoparticles and the N-rich hollow carbon sphere surface. The interaction promotes the transfer of electrons from the N-doped HCSs to the Co oxide particles making them more difficult to reduce (i.e. the reduction peaks shift to higher T). [45]

The post-synthesis functionalization procedure also affected the methanation characteristics of the carbon supports. The signals for the N-doped materials appeared to be shifted to higher temperatures cor-responding to the doped nitrogen content. As a result, the pristine HCS-supported catalyst had the lowest methanation temperature (ca. 653 °C). Notably, the occurrence of the negative methanation peak at high temperatures confirmed that the catalysts would be stable under the reducing conditions present during FT synthesis.

The reducibility of cobalt oxide dispersed on a pristine support when loaded onto hollow carbon spheres with a high nitrogen content was monitored by in situ PXRD measurements. Data collection was done in the temperature range 150–550 °C with 50 °C intervals between successive measurements. Fig. 9 depicts in situ PXRD reduction patterns for 10Co/HCSs and 10Co/N−HCSs$_{600}$ samples. Both sets of data show that the spinel phase of cobalt oxide (Co_3O_4) was the stable phase at T < 250 °C. Reduction of Co at higher temperatures followed the well-established stepwise transformation of cobalt oxide: Co_3O_4 → CoO then CoO → Co°. However, the transformations were noted to occur at dif-ferent temperatures for the two samples. Both reduction steps appeared to be delayed on the 10Co/N−HCSs$_{600}$ catalyst. As an illustration, the CoO to Co° reduction step has been circled to highlight the lower re-duction temperature seen on the pristine HCSs-supported nanoparticles. The CoO → Co° transformation commenced at T = 550 °C for the 10Co/ N−HCSs$_{600}$ sample while it was seen to start occurring at 500 °C for the 10Co/HCSs catalyst. Furthermore, the CoO → Co° reduction was still not complete on the 10Co/N−HCSs$_{600}$ catalyst at the end of the in situ studies as traces of the CoO phase are still visible (Fig. 9b). The slightly higher oxide reduction temperatures seen by in situ PXRD (and H_2-TPR) on the post-synthesis functionalized materials can be attributed to electron transfer from the N-doped carbons to the cobalt catalysts. Yang et al. have used Co 2p XPS and electron paramagnetic resonance

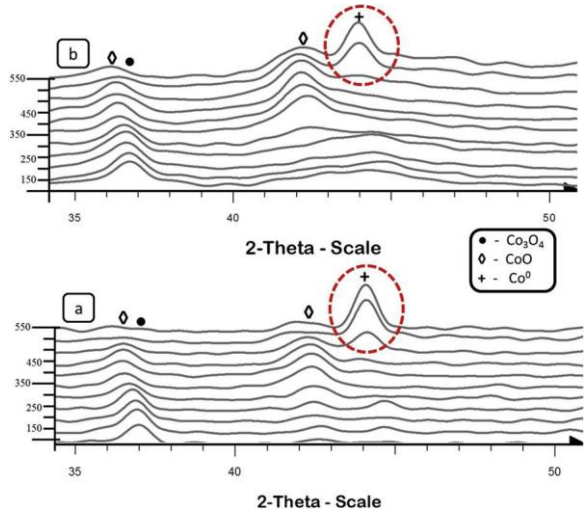

Fig. 9. In situ PXRD patterns of (a) 10Co/HCSs and (b) 10Co/N−HCSs$_{600}$.

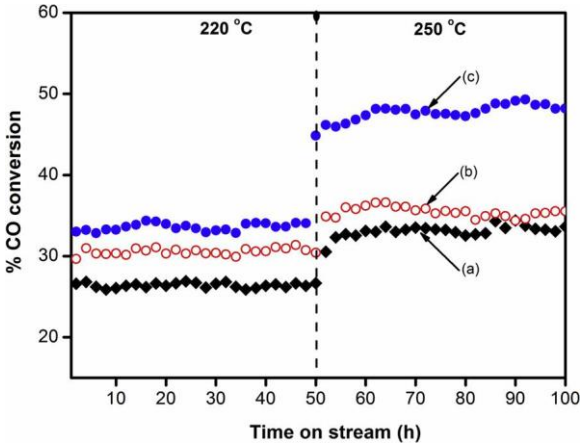

Fig. 10. CO conversions for the Co catalysts supported on pristine and N-doped supports; (a) 10Co/HCSs, (b) 10Co/N−HCSs$_{600}$, and (c) 10Co/N−HCSs$_{900}$, (P = 10 bar, H_2/CO = 2).

techniques to illustrate the electron transfer from N-doped mesoporous carbon to a Co oxide FT catalyst. The electron transfer effect was also observed to shift reduction peaks to higher temperatures, and their findings are in agreement with results reported in this study. [45]

3.5. Fischer-Tropsch evaluation

All the calcined catalysts were reduced in situ with pure H_2 (UHP grade) at 350 °C prior to Fischer-Tropsch catalytic tests at 220 and 250 °C under a similar set of reaction conditions: P = 10 bar, H_2/ CO = 2. Catalyst activity has been expressed as both CO conversion and the cobalt-weight based activity (cobalt time yield, CTY). The CTY is expressed as the mol of CO converted per unit time, per mass of cobalt. Evidently all the catalysts had stable activities at both reaction tem-peratures as shown by the steady CO conversions for the entire period over which this study was conducted (Fig. 10, Table 4). The catalysts maintained their structural integrity during the reaction (vide infra for details on the spent catalysts). The catalysts supported on nitrogen-doped hollow carbon spheres (10Co/N−HCSs$_{600}$, 10Co/N−HCSs$_{900}$) displayed higher CO conversions than the catalyst supported on the undoped support (10Co/HCSs). This trend was consistent under both reaction temperatures and can be attributed to the smaller particle sizes present on the doped supports as observed by both TEM and PXRD techniques. Further, as a consequence of the small cobalt oxide particle sizes on N-doped HCSs, the catalysts had a higher dispersion as con-firmed by SEM and TEM analysis. It was noted that the presence of any strong metal-support interactions on the N-doped supports was com-pensated for by the size of cobalt particles on these catalysts hence they had better activities than the undoped catalyst. For the catalysts sup-ported on functionalized supports, it was observed that a higher ni-trogen content did not necessarily yield the highest activity. It is

Table 4
FT synthesis activity and product distribution for the different catalysts.

Catalyst	Temp.(°C)	% CO conversion	CTY (10^{-5} mol CO/ g_{Co}·s)	Hydrocarbon selectivity (%)		
				C_1	C_2-C_4	C_{5+}
10Co/HCSs	220	26	2.7	13.4	7.9	78.7
	250	33	3.4	22.8	29.9	47.3
10Co/N-HCSs$_{600}$	220	30	3.1	18.5	18.3	63.2
	250	36	3.7	21.9	18.5	59.6
10Co/N-HCSs$_{900}$	220	34	3.5	15.7	8.5	75.8
	250	48	4.9	26.2	21.0	52.8

evident that the strong metal-support interactions seen during TPR studies resulted in a lower activity for the 10Co/N−HCSs$_{600}$ catalyst. In addition, the activity of this catalyst could be lower because the average particle size for this catalyst was smaller than 6 nm which has been shown to be a critical Co size for Fischer-Tropsch catalysis. [6]

Previous studies comparing FT activities for 10 wt% Fe catalysts dispersed on N-doped and undoped carbon nanotubes (CNTs) reported a continuous decrease in activity with time on stream for the sample supported on the pristine carbon support. [21] The undoped catalyst was reported to have a 1.6 times lower activity than its N-doped counterpart. This behaviour was ascribed to significant catalyst sin-tering which occurred at high reaction temperatures on pristine carbon materials. In contrast in this study, catalysts dispersed on the pristine support displayed a stable activity with time on stream which was at-tributed to the unique properties of hollow carbon spheres. HCSs pos-sess a low density and a high surface area which allows for higher dispersions of the catalyst particles on the support which consequently minimizes catalyst agglomeration and favours stable CO conversions during FT synthesis.

To understand the origin of this behaviour, it is to be noted that pristine carbon materials are usually regarded as showing a poor in-teraction with a metal particle. However, it is now accepted that doped carbons are "non-innocent" because they can contribute to the perfor-mance and general characteristics of a catalyst. These doped carbons are analogous to ligands around a metal center of a homogeneous catalyst system, capable of altering the electron density of metal na-noparticles. For instance, the delocalized sp^2 electrons in N-doped carbons can act as a "ligand" by effectively stabilizing metallic nano-particles via electron transfer. [19] Indeed, density functional theory calculations have also been used to observe an intermediate state in-volving a weak hydrogen bond to the carbon support of a Ni-carbon catalyst for methanol decomposition. [46]

Table 4 depicts the hydrocarbon selectivities for the different cata-lysts evaluated at 220 and 250 °C. Comparison of the product se-lectivities for the catalysts at 220 °C revealed that the Co supported on the pristine hollow carbon spheres had the highest C_{5+} selectivity and a low C_1 selectivity. As expected, there was a significant decrease in the C_{5+} selectivity when FT synthesis was carried out at 250 °C for this sample. It must be noted that typical Co FT synthesis is performed in the 220–240 °C temperature range, but a 250 °C reaction temperature has been evaluated in this study to accelerate possible catalyst sintering. On the N-doped samples, comparatively lower C_{5+} values were obtained while the selectivity towards C_1 increased. It was interesting to note that the C_{5+} selectivity did not decrease drastically at 250 °C for the N-doped samples, and the C_1 fraction showed only a slight increase at the elevated reaction temperature.

Previous studies by Borg et al. on Co/γ-Al_2O_3 catalysts have also shown that there tends to be an increase in the C_{5+} product fraction with an increase in the Co particle size, with the highest C_{5+} values possible in the 7–8 nm size range. [47] In another study similar con-clusions were drawn on the Co particle size effect using Co/δ-Al_2O_3 and Co/θ-Al_2O_3 catalysts. [48] In agreement with these reports, the 10Co/ HCSs catalyst had the highest C_{5+} product fraction in this work and the average Co particle size was determined to be 7.7 nm by TEM analysis. It was observed that the C_{5+} selectivities on the studied catalysts were generally low due to fact that these samples were unpromoted and also possibly due to the pore structure of the hollow carbon supports uti-lised. By comparing cobalt catalysts dispersed on γ-Al_2O_3 supports with narrow pores (7 nm) and wide pores (13 nm), Rytter and co-workers demonstrated that wide pores favour higher C_{5+} selectivities. [49] The pore sizes for catalysts in this study were less than 5 nm (Table 4). Due to the comparably smaller size of the hydrogen molecule relative to carbon monoxide, H_2 tends to diffuse much more quickly than CO in the reactor which yields higher H_2/CO ratios in certain parts of the catalyst. A higher H_2 to CO ratio favours chain termination over chain propa-gation resulting in a lower C_{5+} selectivity. Furthermore, the higher methane fraction measured in this work on the N-doped samples is in agreement with conclusions made by Bezemer on C_1 selectivity for small Co nanoparticles. [6]

3.6. The spent catalyst

Catalyst sintering is an important phenomenon in FT synthesis and has been proposed as one of the major deactivation mechanisms in the FT process, alongside poisoning, reoxidation, catalyst surface re-arrangement, water partial pressure, carbon effects (e.g. carbidization, coking or fouling), attrition and the formation of metal-support com-pounds. [50,51] Several studies have shown the loss of catalytically active cobalt surface area due to particle growth under realistic FT re-action conditions. The tendency of smaller particles to sinter and form bigger ones is driven by thermodynamic principles associated with the lower surface energy of larger particles. Notably, sintered catalysts have lower surface concentrations of the catalytic Co phase and thus display poor performances in FT synthesis. Sintering is believed to occur by the coalescence and Ostwald ripening mechanisms. [52–54]

After catalytic evaluations under Fischer-Tropsch conditions, the samples were subsequently studied to evaluate changes which might have occurred during the reaction. Fig. 11 shows TEM images and corresponding particle size distributions measured on the spent cata-lysts after 100 h on stream. It can be seen that the hollow carbon sphere support maintains its structural integrity even after a 100 h exposure to the high pressures and temperatures used during the FT process. Carbon breakage or fracturing was not detected on the pristine or the nitrogen doped support materials. This demonstrates the robustness of the hollow carbon spheres despite their having a thin 30 nm carbon shell. It was also interesting to note that the N-doped materials demonstrated equally good robustness under FT conditions. This observation also confirms that post-synthesis N-doping only introduced marginal defects or structural changes on the carbon framework, and is in agreement with the Raman spectroscopy and XPS data discussed earlier.

The Co particle size distributions on the spent catalysts were also measured and are displayed in Fig. 11b and Fig. 11d. It was noted that the average Co particle size increased for all the samples indicating that sintering had occurred during the catalytic reaction. The minimal sin-tering behaviour observed on these samples is attributed to the hollow carbon supports which offer more accessible surface per unit mass re-lative to conventional support materials. For example, the average particle size on the 10Co/HCSs sample increased from 7.7 to 10.2 nm after 100 h on stream. The insert in Fig. 11a shows that the sintered particles formed a core-shell structure with the reduced cobalt being encapsulated by an outer shell which is composed of oxidized cobalt.

The catalysts supported on N-doped HCSs still had the smaller metal particles after FT synthesis. In particular, the average Co particle size increased from 6.4 to 8.9 nm on the 10Co/N−HCSs$_{900}$ spent catalyst (Fig. 11d). The smaller particles seen for the catalysts supported on the N-doped carbons is consistent with conclusions made in other reports that nitrogen atoms (or the C–N bonds) act as anchoring sites and this immobilizes the catalyst particles even at high reaction temperatures. Notably, the N−HCSs-supported cobalt also had a narrow size dis-tribution even on the spent catalyst with most particles being less than 15 nm, while pristine HCSs-supported cobalt displayed a wider size distribution on the spent catalyst with a significant percentage of crystallites with sizes greater than 20 nm. In another study comparing the FT performance of Fe on N-doped solid carbon spheres prepared by chemical vapour deposition (vertical, horizontal) and hydrothermal synthesis, Xiong et al. reported much greater particle size increases on the spent catalysts. [55] Particle sizes in the 20–40 nm range were measured for the Fe catalyst supported on CVD-prepared (horizontal) support material, despite only having a 5 wt% metal loading. [55] The surface areas of these solid carbon spheres were also low (< 20 m^2/g).

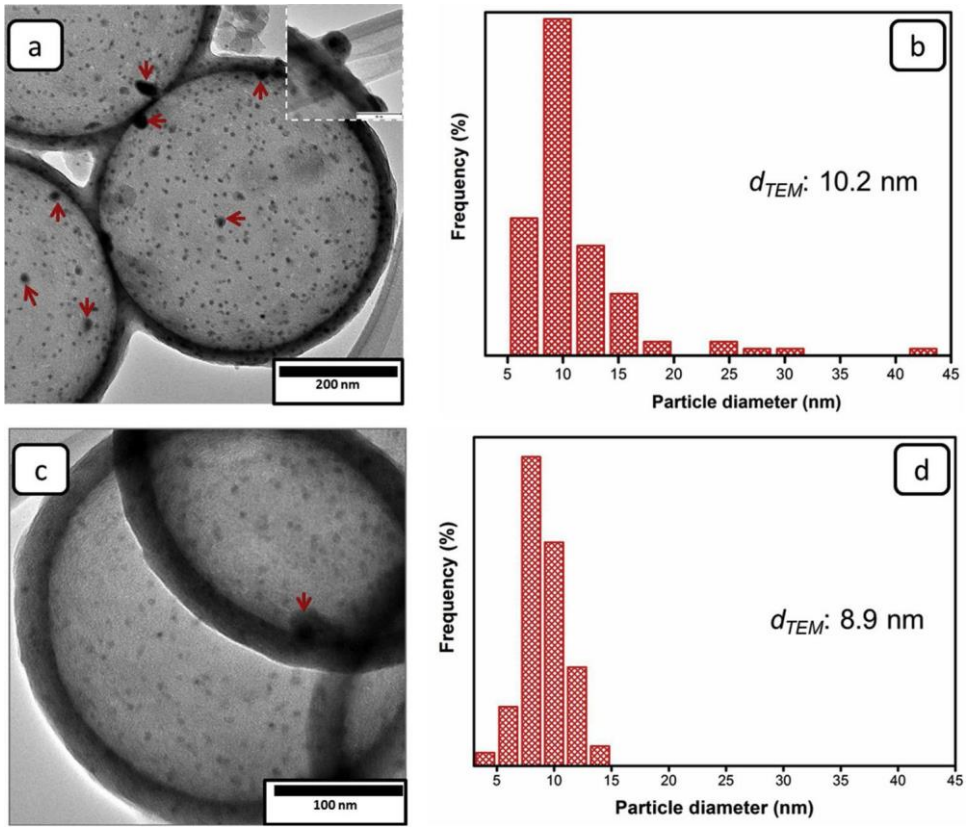

Fig. 11. TEM images of spent catalysts, (a) 10Co/HCSs, (c) 10Co/N−HCSs$_{900}$. The corresponding particle size distributions are displayed in (b) and (d). (Insert) A high magnification image of the spent Co catalyst supported on pristine hollow carbon spheres i.e. 10Co/HCS sample.

4. Conclusions

In this study we have used hollow carbon spheres as catalyst sup-ports and shown that they are a suitable model support material for cobalt Fischer-Tropsch catalysts. Synthesis of these materials via a solid template approach was shown to yield uniform and monodispersed HCSs with high specific surface areas and good thermal stabilities. More interestingly, a strategy for the surface N-functionalization of the ma-terials by a method which involves the addition of a nitrogen source onto an already prepared carbon framework has been demonstrated. This simple procedure provided a unique material which is favourable for use as a carbon support for several reasons; (1) it has more catalyst anchoring sites, (2) its thermal stability is comparable to those for the pristine material hence its mechanical strength is not compromised, and
(3) it immobilized the catalyst nanoparticles during the reaction leading to minimized particle agglomeration. Results from this study also showed that the surface properties of materials produced by this strategy are dependent on the carbonization temperature. These surface properties were shown to influence the metal-support interactions on the prepared catalysts. Thus the carbonization temperature can be used to tune the strength of metal-support interactions in such materials. N-functionalization effects were also evident in FT synthesis and yielded catalysts with improved activities and stabilities. We believe that the catalyst stabilizing effect produced by the post-synthesis melamine in-troduction to already prepared carbons can also be used to anchor other types of catalysts on carbon supports synthesized using a similar ap-proach.

Acknowledgements

The authors want to thank the University of the Witwatersrand, the NRF and the DST-NRF Centre of Excellence in Catalysis (c*change) for financial support. Professor Sekhar C. Ray (University of South Africa) is acknowledged for assistance with XPS measurements.

References

[1] S. Chu, A. Majumdar, Nature 488 (2012) 294–303.
[2] C. Wei, Z. Bart, F.I. A. W, P. Robert, H.E. J. M, ChemCatChem 10 (2018) 136–140.
[3] V.R. Calderone, N.R. Shiju, D. Curulla-Ferré, S. Chambrey, A. Khodakov, A. Rose, J. Thiessen, A. Jess, G. Rothenberg, Angew. Chem. Int. Ed. 52 (2013) 4397–4401.
[4] F. Morales, F.M.F. de Groot, O.L.J. Gijzeman, A. Mens, O. Stephan, B.M. Weckhuysen, J. Catal. 230 (2005) 301–308.
[5] E. Iglesia, Appl. Catal. A Gen. 161 (1997) 59–78.
[6] G.L. Bezemer, J.H. Bitter, H.P.C.E. Kuipers, H. Oosterbeek, J.E. Holewijn, X. Xu, F. Kapteijn, A.J. van Dillen, K.P. de Jong, J. Am. Chem. Soc. 128 (2006) 3956–3964.
[7] G.L. Bezemer, T.J. Remans, A.P. van Bavel, A.I. Dugulan, J. Am. Chem. Soc. 132 (2010) 8540–8541.
[8] M.E. Dry, Appl. Catal. A Gen. 276 (2004) 1–3.
[9] M. Rahmati, B. Huang, M.K. Mortensen, K. Keyvanloo, T.H. Fletcher, B.F. Woodfield, W.C. Hecker, M.D. Argyle, J. Catal. 359 (2018) 92–100.
[10] H.M. Torres Galvis, J.H. Bitter, C.B. Khare, M. Ruitenbeek, A.I. Dugulan, K.P. de Jong, Science 335 (2012) 835–838.
[11] Y. Piao, K. An, J. Kim, T. Yu, T. Hyeon, J. Mater. Chem. 16 (2006) 2984.
[12] G. Wu, Y. Cheng, Z. Yang, Z. Jia, H. Wu, L. Yang, H. Li, P. Guo, H. Lv, Chem. Eng. J. 333 (2018) 519–528.
[13] L. Kong, X. Yin, M. Han, X. Yuan, Z. Hou, F. Ye, L. Zhang, L. Cheng, Z. Xu, J. Huang, Carbon 111 (2017) 94–102.
[14] L. Kong, C. Wang, X. Yin, X. Fan, W. Wang, J. Huang, J. Mater. Chem. C Mater. Opt. Electron. Devices 5 (2017) 7479–7488.
[15] T.N. Phaahlamohlaka, D.O. Kumi, M.W. Dlamini, L.L. Jewell, N.J. Coville, Catal. Today 275 (2016) 76–83.
[16] H. Xu, X. Yin, M. Li, F. Ye, M. Han, Z. Hou, X. Li, L. Zhang, L. Cheng, Carbon 132 (2018) 343–351.
[17] M.W. Dlamini, D.O. Kumi, T.N. Phaahlamohlaka, A.S. Lyadov, D.G. Billing, L.L. Jewell, N.J. Coville, ChemCatChem 7 (2015) 3000–3011.
[18] S. Campisi, C. Chan-Thaw, A. Villa, Appl. Sci. Basel (Basel) 8 (2018) 1159.
[19] M. Antonietti, M. Oschatz, Adv. Mater. 30 (2018) 1706836.
[20] C. Galeano, J.C. Meier, M. Soorholtz, H. Bongard, C. Baldizzone, K.J.J. Mayrhofer, F. Schüth, ACS Catal. 4 (2014) 3856–3868.
[21] J. Lu, L. Yang, B. Xu, Q. Wu, D. Zhang, S. Yuan, Y. Zhai, X. Wang, Y. Fan, Z. Hu, ACS Catal. 4 (2014) 613–621.
[22] H.J. Schulte, B. Graf, W. Xia, M. Muhler, ChemCatChem 4 (2012) 350–355.

[23] J. Xie, J. Yang, A.I. Dugulan, A. Holmen, D. Chen, K.P. de Jong, M.J. Louwerse, ACS Catal. 6 (2016) 3147–3157.
[24] H. Xiong, M. Moyo, M.K. Rayner, L.L. Jewell, D.G. Billing, N.J. Coville, ChemCatChem 2 (2010) 514–518.
[25] X. Chen, D. Deng, X. Pan, Y. Hu, X. Bao, Chem. Commun. 51 (2015) 217–220.
[26] M. Luo, H. Li, React. Kinet. Mech. Catal. 124 (2018) 279–291.
[27] S. Maldonado, K.J. Stevenson, J. Phys. Chem. B 109 (2005) 4707–4716.
[28] B. Stohr, H.P. Boehm, R. Schlogl, Carbon 29 (1991) 707.
[29] H. Xiong, M.A. Motchelaho, M. Moyo, L.L. Jewell, N.J. Coville, Appl. Catal. A Gen. 482 (2014) 377–386.
[30] S. Feng, W. Li, Q. Shi, Y. Li, J. Chen, Y. Ling, A.M. Asiri, D. Zhao, Chem. Commun. 50 (2014) 329–331.
[31] A.B. Fuertes, P. Valle-Vigon, M. Sevilla, Chem. Commun. 48 (2012) 6124–6126.
[32] X. Duan, Z. Ao, H. Sun, S. Indrawirawan, Y. Wang, J. Kang, F. Liang, Z.H. Zhu, S. Wang, ACS Appl. Mater. Interfaces 7 (2015) 4169–4178.
[33] X. Li, H. Wang, J.T. Robinson, H. Sanchez, G. Diankov, H. Dai, J. Am. Chem. Soc. 131 (2009) 15939–15944.
[34] Y. Li, Y. Zhao, H. Cheng, Y. Hu, G. Shi, L. Dai, L. Qu, J. Am. Chem. Soc. 134 (2012) 15–18.
[35] J. Liu, Q. Li, Y. Zou, Q. Qian, Y. Jin, G. Li, K. Jiang, S. Fan, Nano Lett. 13 (2013) 6170–6175.
[36] L. Chen, P. Hu, C.P. Deming, N. Wang, J.E. Lu, S. Chen, J. Phys. Chem. C 120 (2016) 13303–13309.
[37] A.G.S. Filho, A. Jorio, G.S. Ge, G. Dresselhaus, R. Saito, M.S. Dresselhaus, Nanotechnology 14 (2003) 1130.
[38] W. Ding, Z. Wei, S. Chen, X. Qi, T. Yang, J. Hu, D. Wang, L.-J. Wan, S.F. Alvi, L. Li, Angew. Chem. 125 (2013) 11971–11975.
[39] J. Zhang, L. Ma, M. Gan, F. Yang, S. Fu, X. Li, J. Power Sources 288 (2015) 42–52.
[40] S. Marzorati, J.M. Vasconcelos, J. Ding, M. Longhi, P.E. Colavita, J. Mater. Chem. A Mater. Energy Sustain. 3 (2015) 18920–18927.
[41] X.Y. Chen, C. Chen, Z.J. Zhang, D.H. Xie, Ind. Eng. Chem. Res. 52 (2013) 12025–12031.
[42] M. Seredych, D. Hulicova-Jurcakova, G.Q. Lu, T.J. Bandosz, Carbon 46 (2008) 1475–1488.
[43] T. Fu, R. Liu, J. Lv, Z. Li, Fuel Process. Technol. 122 (2014) 49–57.
[44] G. Prieto, P. Concepción, R. Murciano, A. Martínez, J. Catal. 302 (2013) 37–48.
[45] Y. Yang, L. Jia, B. Hou, D. Li, J. Wang, Y. Sun, J. Phys. Chem. C 118 (2014) 268–277.
[46] Z.-H. Xue, J.-T. Han, W.-J. Feng, Q.-Y. Yu, X.-H. Li, M. Antonietti, J.-S. Chen, Angew. Chem. Int. Ed. 57 (2018) 2697–2701.
[47] Ø. Borg, P.D.C. Dietzel, A.I. Spjelkavik, E.Z. Tveten, J.C. Walmsley, S. Diplas, S. Eri, A. Holmen, E. Rytter, J. Catal. 259 (2008) 161–164.
[48] S. Rane, Ø. Borg, E. Rytter, A. Holmen, Appl. Catal. A Gen. 437–438 (2012) 10–17.
[49] E. Rytter, S. Eri, T.H. Skagseth, D. Schanke, E. Bergene, R. Myrstad, A. Lindvåg, Ind. Eng. Chem. Res. 46 (2007) 9032–9036.
[50] H. Karaca, O.V. Safonova, S. Chambrey, P. Fongarland, P. Roussel, A. Griboval-Constant, M. Lacroix, A.Y. Khodakov, J. Catal. 277 (2011) 14–26.
[51] H. Karaca, J. Hong, P. Fongarland, P. Roussel, A. Griboval-Constant, M. Lacroix, K. Hortmann, O.V. Safonova, A.Y. Khodakov, Chem. Commun. (Camb.) 46 (2010) 788–790.
[52] K.H. Cats, J.C. Andrews, O. Stephan, K. March, C. Karunakaran, F. Meirer, F.M.F. de Groot, B.M. Weckhuysen, Catal. Sci. Technol. (2016), https://doi.org/10.1039/c1035cy01524c.
[53] M. Sadeqzadeh, J. Hong, P. Fongarland, D. Curulla-Ferré, F. Luck, J. Bousquet, D. Schweich, A.Y. Khodakov, Ind. Eng. Chem. Res. 51 (2012) 11955–11964.
[54] D. Kistamurthy, A.M. Saib, D.J. Moodley, J.W. Niemantsverdriet, C.J. Weststrate, J. Catal. 328 (2015) 123–129.
[55] H. Xiong, M. Moyo, M.A. Motchelaho, Z.N. Tetana, S.M.A. Dube, L.L. Jewell, N.J. Coville, J. Catal. 311 (2014) 80–87.